NUCL SCI TECH (2019) 30:50
https://doi.org/10.1007/s41365-019-0561-y

Beam and image experiment of beam deflection electron gun for distributed X-ray sources

Cheng-Jun Tan[1,2] · Chuan-Xiang Tang[1,2] · Wen-Hui Huang[1,2] · Qing-Xiu Jin[1,2] · Ying-Chao Du[1,2] · Qun Luo[3] · Pei-Dong Wu[3] · Dong-Hai Liu[3] · Lu-Ming Zhang[3] · Cong Xu[3]

Received: 4 May 2018 / Revised: 12 September 2018 / Accepted: 13 September 2018 / Published online: 19 February 2019

Abstract Distributed X-ray sources comprise a single vacuum chamber containing multiple X-ray sources that are triggered and emit X-rays at a specific time and location. This process facilitates an application for innovative system concepts in X-ray and computer tomography. This paper proposes a novel electron beam focusing, shaping, and deflection electron gun for distributed X-ray sources. The electron gun uses a dispenser cathode as an electron emitter, a mesh grid to control emission current, and two electrostatic lenses for beam shaping, focusing, and deflection. Novel focusing and deflecting electrodes were designed to increase the number of focal spots in the distributed source. Two identical half-rectangle opening electrodes are controlled by adjusting the potential of the two electrodes to control the electron beam trajectory, and then, multifocal spots are obtained on the anode target. The electron gun can increase the spatial density of the distributed X-ray sources, thereby improving the image quality. The beam experimental results show that the focal spot sizes of the deflected (deflected amplitude 10.5 mm) and non-deflected electron beams at full width at half maximum are 0.80 mm $\times$ 0.50 mm and 0.55 mm $\times$ 0.40 mm, respectively (anode voltage 160 kV; beam current 30 mA). The imaging experimental results demonstrate the excellent spatial resolution and time resolution of an imaging system built with the sources, which has an excellent imaging effect on a field-programmable gate array chip and a rotating metal disk.

Keywords Beam deflection electron gun · X-ray imaging · Distributed X-ray sources · Stationary CT

✉ Chuan-Xiang Tang
tang.xuh@tsinghua.edu.cn

Cheng-Jun Tan
cdut.tchj@foxmail.com

1 Accelerator Laboratory, Department of Engineering Physics, Tsinghua University, Beijing 100084, China

2 Key Laboratory of Particle and Radiation Imaging, Ministry of Education, Tsinghua University, Beijing 100084, China

3 Nuctech Company Limited, Beijing 100084, China

1 Introduction

Spiral computer tomography (spiral CT) [1–4] is currently the most common and state-of-the-art imaging application. However, spiral CT has several inherent defects. First, the X-ray source continuously spins at a high speed throughout the scanning process, resulting in large effective focal spots. Second, the X-ray source, high-voltage power, and cooling system on the slip ring slow down the rotation. The fastest rotation of a commercial spiral CT is 4 Hz, which is not suitable for imaging a dynamic process or moving objects [5]. Stationary CT [6] replaces the slip ring of the spiral CT with an array of X-ray sources and controls the sources to operate in a set sequence to scan an object from different angles. The scanning process is shown in Fig. 1. The electronic switch replaces the mechanical rotation of the spiral CT. This part greatly improves the scan efficiency and eliminates the motion artifact. The stationary CT device features the following advantages [7, 8]. Firstly, it increases the overall power of the source and improves the contrast ratio. Secondly, it provides more imaging information. Thirdly, it can reduce the X-ray dose on the inspected object by optimizing the imaging system. Therefore, the stationary CT has great

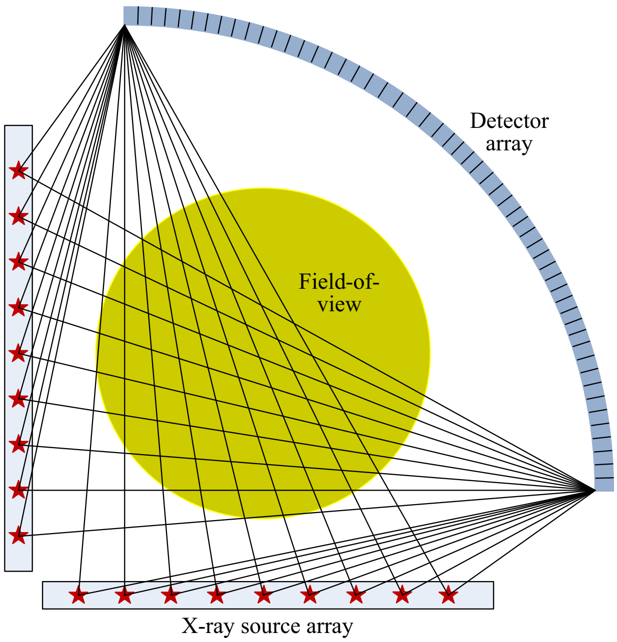

Fig. 1 (Color online) Stationary CT conceptual diagram

potential for industrial nondestructive inspection and medical CT imaging [9].

The array of X-ray sources in stationary CT is called distributed X-ray sources or a multisource. Each X-ray source has an independent cathode, electron beam control electrode, and focusing electrode. The structure is shown in Fig. 2, in which the electron gun is an electron emitter that contains the cathode, electron beam control electrode, and focusing electrode. During operation, the system controls the electron guns to emit electrons by presetting the time order, which obtains energy from the high-voltage electric field and generates an X-ray on the anode target. At present, distributed X-ray sources for security inspection CT require a high voltage of approximately 160 kV and a beam current of not more than 30 mA.

In 2014, Schwoebel et al. used the Spindt emitter [10, 11] to design a multisource for human mammary gland and small animal imaging. The multisource had 10 cathodes, with a highest energy of 50 keV and a beam current of 10 mA [12]. The experimental results demonstrated that the Spindt emitter had low stability and a short life span, but high costs and vacuum requirements. In 2009, Qian et al. designed a multisource by combining 31 carbon nanotube (CNT) cathodes [13] with the highest energy of 160 keV and the largest power of 3 kW [14, 15]. The experiment result demonstrated that the emission capability of the CNT cathode was insufficient and fluctuated downwardly with time [13, 16, 17]. A feedback should be provided to adjust the grid voltage, and this requirement increases the complexity of the system [16, 18]. In 2014, GE designed a multisource for medical CT imaging. This multisource has 32 thermal cathodes, with a largest energy of 140 keV and a largest beam current of 500 mA [19–21].

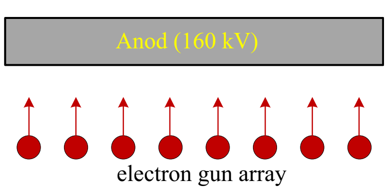

Fig. 2 (Color online) Distributed X-ray source diagram

In this study, the cold cathode (Spindt and CNT [13, 17]) is eliminated because of its low emission capability and poor stability. A dispenser cathode is characterized by a lower working temperature, a greater emission current, and a longer life span. This cathode can also be reactivated when exposed to air. These advantages facilitate the application of a dispenser cathode as a good electron emitter for commercial distributed X-ray sources. Therefore, in this study, a dispenser cathode is adopted in the design of a beam deflection electron gun with a diameter of 3.2 mm and a working temperature of 1000 °C.

2 Structure and mechanism of the electron gun

Figure 2 shows the overall structure of the distributed X-ray sources. The electron gun is one of the most crucial parts, and it determines important features, such as source intensity and focal spot. The physical design of the gun is accomplished using CST Particle studio, which is a professional electromagnetic field analysis tool.

The electron gun features include electron beam extraction, transfer, focusing, and deflection. The beam can be extracted and controlled with the grid and pore electrodes. The pore electrode presents the advantage of having no electron beam interception on the electrode. Meanwhile, in the grid electrode, the voltage of its grid mesh is 6–7 times lower than that of the pole electrode, to obtain the same electric field on the cathode surface. However, the grid electrode intercepts part of the electrons. Thus, the beam extracting voltage and the complexity of the control system are reduced by installing an electron gun with the grid mesh as the beam extraction electrode.

Because the mesh is a nonlinear element, after the beam passes through the mesh, the beam emittance grows. To minimize the emittance growth, an electrode is installed behind the mesh, and when the electrode potential is set at a right value such that the electric fields on both sides of the mesh are roughly equal, the beam emittance is minimized. This electrode, which is aimed to adjust the emittance of the beam, is called the emittance compensation electrode (ECE; Fig. 3) [19].

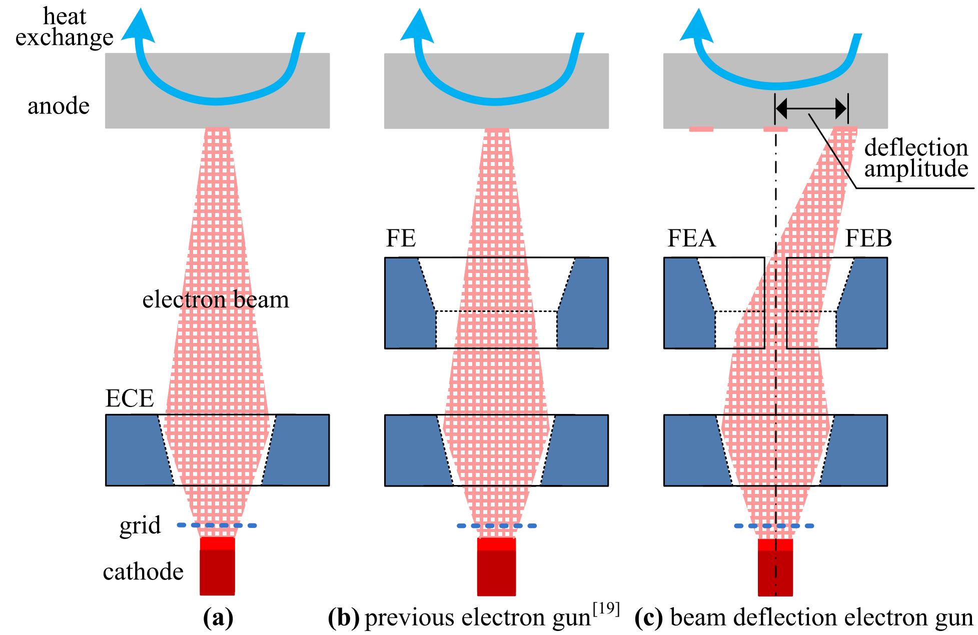

Fig. 3 (Color online) Schematic of electron gun structure

No other electrode is assumed to exist after the ECE (Fig. 3a). In this case, the beam can obtain an ideal focal spot by adjusting the ECE potential. However, the other parameters, such as grid current (the electron beam intercepted by the mesh) and ECE current (the electron beam intercepted by the ECE), are difficult to optimize. At the same time, a better focal spot size is difficult to obtain when the beam current is larger. Therefore, a focusing electrode (FE) is designed after the ECE (Fig. 3b). The ECE adjusts the beam emittance, grid current, and ECE current, while the FE optimizes the focal spot size.

The greater the number of X-ray sources is, the better the imaging result will be. Thus, additional imaging information from other angles is provided, thereby improving the imaging quality. The minimum distance between cathodes is set at 20 mm, considering the size of the cathode ceramic component (Fig. 4), ECE, and FE. With the structure of Fig. 3b, there are only 50 cathodes in the source of 1 m, generating no more than 50 X-ray sources. Furthermore, the heating power of a single cathode is approximately 7.2 W and the total power of 50 cathodes is 360 W, thereby increasing the cathode mount (Fig. 4) temperature to as high as 320 °C when all the cathodes are in operation and reach thermal equilibrium, and increasing the outgassing of the cathode mount, which increases the burden of the vacuum system and creates new difficulties in thermal management of the system.

Therefore, a novel beam deflection electron gun structure, as shown in Fig. 3c, is designed. This structure divides the focusing electrode in the middle to obtain two equal parts, namely focusing electrode A (FEA) and focusing electrode B (FEB). If these two focusing electrodes have the same potential, then the focusing effect is equivalent to Fig. 3b. If these two focusing electrodes have different potentials, then the electron beam through the focusing electrode is not only focused, but also deflected. If the potential difference between FEA and FEB is $+V_{\text{defl}}$, $-V_{\text{defl}}$, and 0, the electron beam will be deflected with the potential difference, and then, three different focal spots on the anode target will be obtained. If the deflection amplitude of the electron beam on the anode target is 10 mm and one cathode generates three focal spots, then only 33 cathodes are required in a source of 1 m to generate 99 X-ray sources. This method uses fewer cathodes to obtain more focal spots, which can reduce costs, increase the spatial density of the distributed X-ray

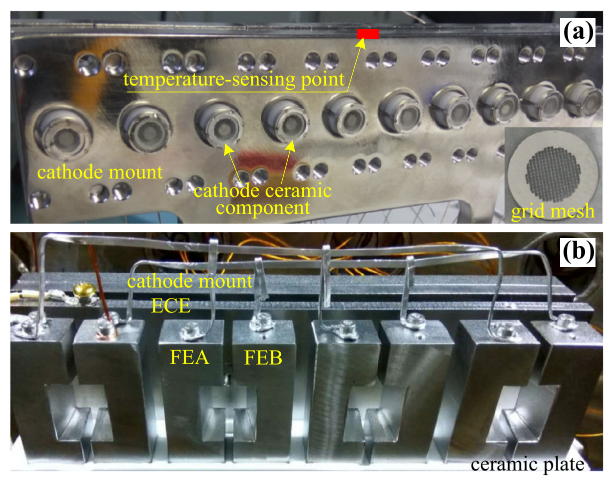

Fig. 4 (Color online) Photograph of the electron gun and its components

sources, and reduce system thermal management difficulty. In addition, one cathode may generate 4, 5, 6, or more focal spots on the anode target by controlling the potential difference of FEA and FEB, thus obtaining a high spatial density distributed X-ray source.

Figure 5 shows the simulation results of the beam emittance after the electron passes through the grid. When the ECE potential is approximately 1.0 kV, the beam emittance is minimized at approximately 47 mm mrad. The simulation conditions are a mesh potential of 50 V, an anode potential of 160 kV, and a beam current of approximately 60 mA. The FEA potential is maintained at 7.0 kV, the FEB potential is changed from 7.0 to 10.0 kV, and the state of the electron beam is changed from non-deflected to deflected, but the beam emittance hardly changes significantly, as shown in Fig. 5. Therefore, the beam emittance after the electrons go through the mesh is not affected by the potential change of FEA and FEB caused by electron beam deflection.

3 Beam experiment of the electron gun

3.1 Cathode features and beam extraction

The dispenser cathode has two working modes, namely temperature-limited and space charge-limited modes. When the cathode operates in the first mode, the emission is mainly controlled by the temperature and the extraction voltage. By contrast, in the second mode, the cathode has sufficient electrons on the surface, and the emission depends on the extraction voltage, rather than the temperature. A grid mesh electrode is installed at approximately 300 μm before the cathode to extract the beam. No electron is emitted from the cathode when the grid mesh has a negative potential. By contrast, when the grid mesh has a positive potential, the cathode emits electrons, and the current is proportional to three-second power of the grid mesh potential (Fig. 6).

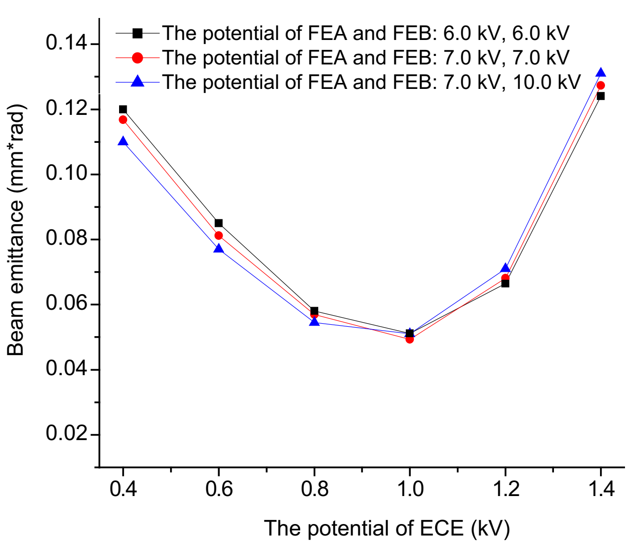

Fig. 5 (Color online) Simulation results of beam emittance after the electrons go through mesh

The grid mesh should be selected according to several factors, such as the grid mesh interception rate, the working voltage of the grid, and the evenness of the electric field on the cathode surface. When the interception rate is larger, the utilization of the beam is smaller, and a large number of electrons hit the grid mesh. This process heats the grid mesh to deform and damage the beam transmission. Therefore, the grid interception rate is minimized as much as possible. However, when the interception is too small, the grid wire will be thinner or the grid-wire spacing will be larger. This characteristic will lead to the unevenness of the electric field on the cathode surface and will diminish the life span of the cathode. In addition, the evenness of the electric field is affected by the distance between the cathode and the grid mesh. Assuming that all physical parameters have been determined, the farther the distance between the grid mesh and the cathode is, the more even the electric field will be. However, the grid voltage will also be higher when the same beam is extracted. A high grid voltage results in a complex control system. Moreover, the higher the voltage grid is, the higher the power of the beam that will hit the grid mesh. This process heats the grid mesh. Hence, molybdenum is selected for the grid mesh of the system. The physical transparency is approximately 76%. The grid mesh is separated by 300 μm from the cathode to ensure the evenness of the electric field on the cathode surface.

Figure 6a shows the relationship between the cathode emission and the grid voltage at different heating powers (temperatures). At a lower heating power (e.g., 5.9 W), the cathode works in the space charge-limited mode if the emission is smaller (< 200 mA). However, the cathode works in the temperature-limited mode if the emission is larger (> 200 mA). According to Fig. 6b, the emission increases with the heating power. When the heating power reaches a value of approximately 7.5 W, the cathode emission increases slowly with the increase in heating power and finally enters a plateau region. However, this characteristic does not indicate that the cathode will work in the turning corner (approximately 7.5 W) of the rising and plateau region. When the heating power is 7.5 W, the cathode functions in the peak emission state with an emission of over 800 mA. In reality, the beam current of the gun is no more than 30 mA. Therefore, the heating power can be reduced. If the heating power is 5.9 W, the cathode functions in the space charge-limited mode when the emission is < 100 mA. At the same time, the heating

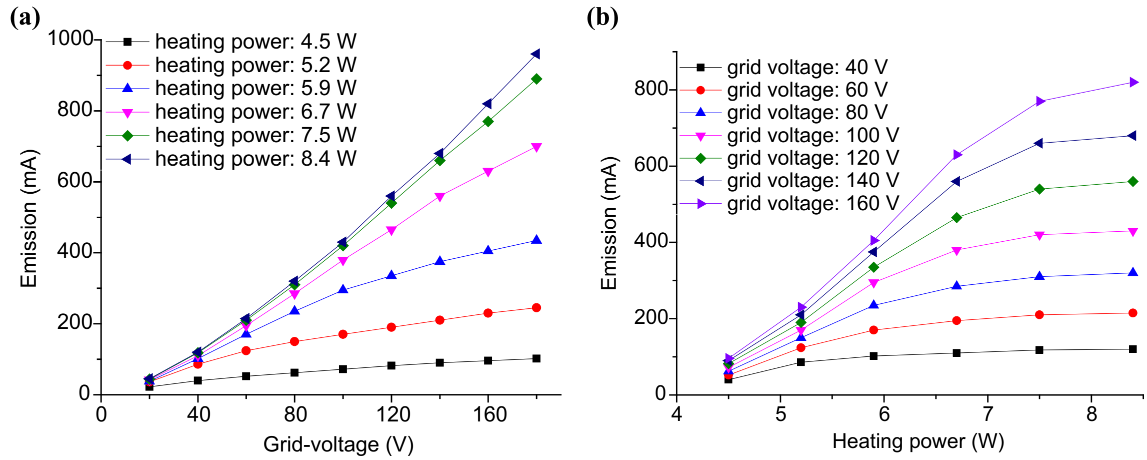

Fig. 6 (Color online) Cathode emission (pulse working, pulse width 100 µs and frequency 50 Hz)

power is 1.6 W lower than 7.5 W. If 50 cathodes are used, the system can save 80 W of heating power. This characteristic not only reduces the system power consumption but also the working temperature. Moreover, the lifetime of the cathode is extended, and the thermal management of the cathode mount is easier.

3.2 Emittance compensation electrode (ECE)

An ECE is designed at approximately 4 mm after the grid mesh to optimize the beam emittance (Fig. 5) and interception rate of the grid mesh (the ratio of the grid current to the emission current). The electrons will pass through the grid mesh at a higher speed as the ECE potential increases. This process reduces the interception rate of the grid mesh and improves the utilization of the beam. More importantly, it can reduce the power of the electrons on the grid mesh and the temperature of the grid mesh. Thus, the deformation and melting of the grid mesh caused by a high temperature are avoided. Figure 7 shows the relationship between the grid mesh interception rate and the ECE potential. The proper increase in the ECE potential can reduce the grid interception rate. Thus, the ECE potential can be appropriately increased when the system is operating.

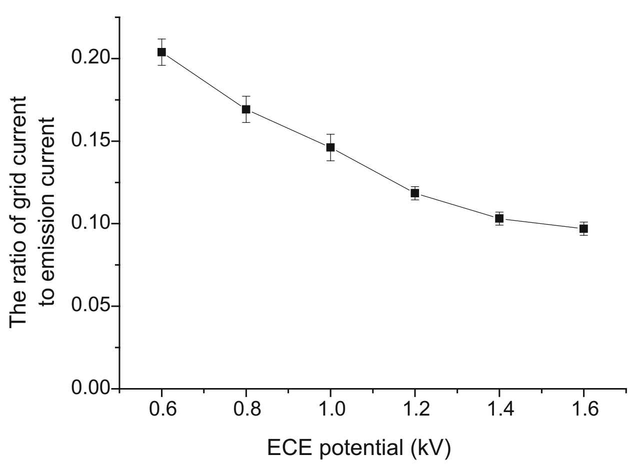

Fig. 7 Relationship between grid interception rate and ECE potential

The ECE potential not only affects the mesh interception rate, but also the ECE current (the beam intercepted by the ECE). During operation, the ECE current is expected to be maintained as low as possible. The ECE current is mainly due to the transverse diffusion of the beam caused by the space charge effect when the electron beam passes through the ECE. It is affected by the emittance when the beam passes through the grid mesh and ECE.

At a lower ECE potential, the emittance growth of the electrons passing through the grid mesh and ECE is larger. This phenomenon results in a larger ECE current. The appropriate improvement of the ECE potential can reduce the emittance of the beam when it goes through the grid mesh and ECE. This process remarkably reduces the ECE current. If the ECE potential is further increased, the emittance of beam through the grid mesh significantly increases, which induces an increase in the ECE current (Fig. 8). An appropriate value of ECE potential (1.0–1.3 kV) exists, at which the ECE current is minimized and the mesh interception is maintained at a lower rate. The experimental conditions are an anode voltage of 160 kV, a cathode emission of approximately 40 mA, and an FE potential of 5.0 kV.

3.3 Deflection amplitude, focal spot, and focusing electrode (FE)

Deflection amplitude is one of the most important features of the beam deflection electron gun. Deflection amplitude is defined as the distance between the focal spots generated on the anode with and without the transverse

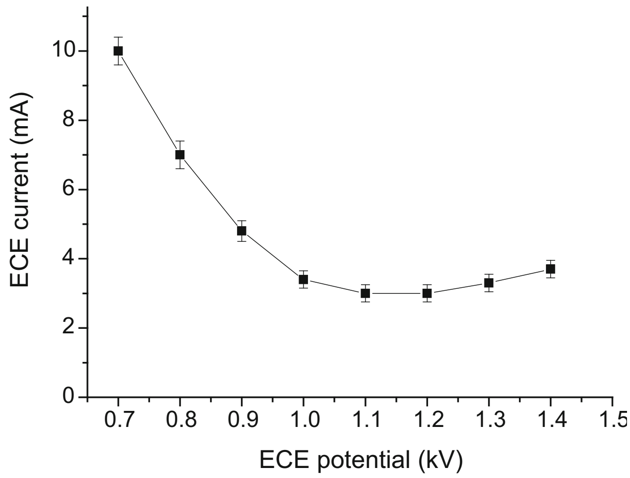

Fig. 8 Relationship between ECE current and ECE potential

deflected electric field, as shown in Fig. 3c. It is related not only to the potential difference between FEA and FEB but also to the potential of FEA (or FEB). Figure 9 shows the relationship between the deflection amplitude and the potential difference of FEA and FEB (potential of FEB minus that of FEA) when the FEA potential has different values. Figure 9 shows that the deflection amplitude and the potential difference are almost in direct proportion and the linear fit is over 0.998. The reason is that the potential difference between FEA and FEB is relatively small (less than 3.5 kV) and the relativistic effect of electron beam in transversal deflection is not remarkable. When the potential difference of the electrodes is same, the higher the FEA potential is, and the smaller the deflection amplitude will be. This is because a higher focusing potential causes a faster speed and a shorter time consumed when the electron beam goes through the focusing electrodes. Thus, the time that the electron beam is exposed to the deflection electric field is shorter, reducing the transversal velocity component when the beam goes through the focusing electrodes, and also reducing the deflection amplitude. The experimental conditions are as follows: ECE potential of 1.1 kV, distance between FEA (or FEB) and anode of 80 mm, anode voltage of 160 kV, beam current of 30 mA, and pulse width of 100 μs. In Fig. 9, the relative error is extremely small; thus, error bars are not shown.

Figure 10 shows the effect of the beam current on the deflection amplitude when the FEA and FEB potentials are 7.0 and 10.0 kV, respectively. The figure demonstrates that the deflection amplitude of the electron beam slightly decreases (i.e., by 2.5%) with increasing beam current. Therefore, the deflection amplitude is not affected by the beam current in a certain range.

Focal spot size is another important feature of the beam deflection electron gun. A focal spot usually includes an actual focal spot and an effective focal spot. The actual focal spot is the area on the anode where an X-ray is produced, and the effective focal spot is the size of the focal spot measured from different directions. In the absence of a special explanation, the focal spot in this paper refers to the effective focal spot. Pinhole imaging is a common method to measure the focal spot. The measurement selects a pinhole with a diameter of approximately 0.15 mm and a thickness of approximately 1.60 mm, and the material is tungsten. The distance from the focal spot to the pinhole is 230 mm, while the distance from the pinhole to the flat detector is 870 mm, and the geometric magnification is approximately 3.8 times. The detector system employs a PaxScan 2520DX flat panel detector from Varian with a resolution of 127 μm and 1920 × 1536 pixels (area of approximately 200 mm × 250 mm). Figure 11 shows a focal spot image taken with the flat panel detector. The focal spot size is calculated by the full width at half maximum (FWHM) of the measurement.

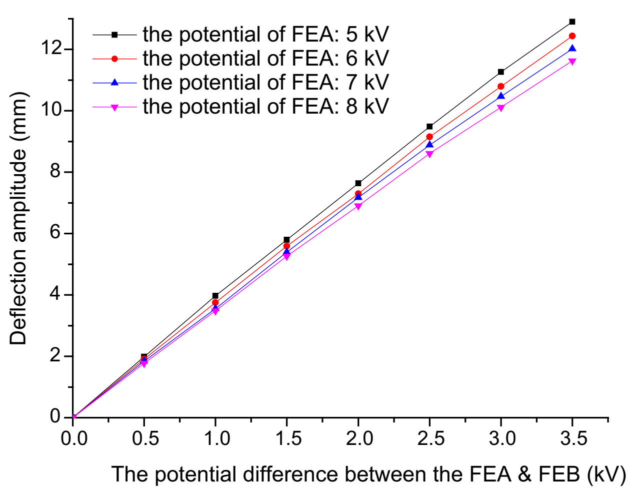

Fig. 9 (Color online) Deflection amplitude variation with the potential difference of FEA and FEB

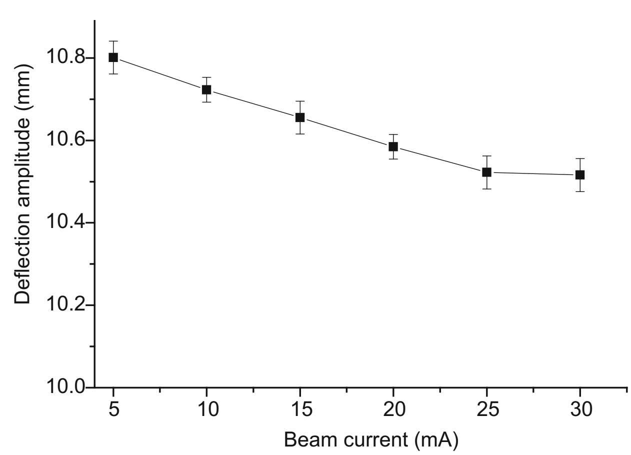

Fig. 10 Deflection amplitude variation with beam current

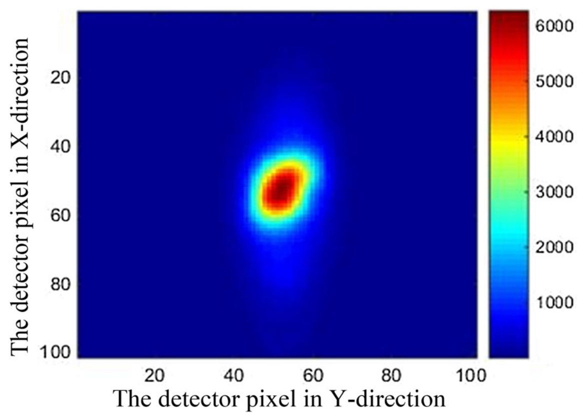

Fig. 11 (Color online) Focal spot image of the electron gun

When the potentials of FEA and FEB are equal, the electron beam will not deflect. Figure 12 shows the relationship between the focal spot size and the focusing potential with different ECE potentials when the electron beam is non-deflected. The experimental conditions are an anode voltage of 160 kV and a beam current of 30 mA. The focal spot size is measured in two directions. The figure only shows the focal spot in the *X*-direction because the size in the *Y*-direction is maintained at a small value of approximately 0.40 mm due to the geometrical compression by the inclination angle of the anode. When the focusing potential is lower, the focusing capability of the focusing electrodes (FEA and FEB) is stronger and the beam over-focuses, causing a larger focal spot. Moreover, when the focusing potential is higher, the focusing capability is weaker and the beam insufficiently focuses, resulting in a larger focal spot. The electron gun has a suitable focusing potential (5.0–5.5 kV) that obtains the optimum focal spot size.

Figures 7 and 8 show that properly increasing the ECE potential facilitates the reduction in the grid and ECE currents but promotes the emittance growth of the beam (Fig. 5). Figure 12 presents that the optimal focal spot sizes are larger at a low or high ECE potential. This phenomenon is due to the fact that after the beam passes through the grid mesh, the emittance becomes larger, and the focusing effect of the beam is poor. The optimal ECE potential (approximately 1.1 kV) allows the system to obtain the optimal focal spot size (approximately 0.55 mm $\times$ 0.40 mm). At this moment, the emittance growth after the beam passes through grid mesh is minimum.

When the potentials of FEA and FEB are different, the electron beam is not only focused but also deflected when it passes through FEA and FEB. Figure 13 shows the focal spot size at different deflection amplitudes but under the same experimental conditions as shown in Fig. 9 (anode voltage of 160 kV and beam current of 30 mA). Figure 13 shows that when the potential of FEA is lower, the focal spot size increases with the increase in the potential difference between FEA and FEB. Moreover, when the potential of FEA is higher, the focal spot size decreases with the increase in the potential difference between FEA and FEB. The reason is because the focusing capability on the beam is the combined result of the ECE and focusing electrodes (FEA and FEB). The ECE potential remains at 1.1 kV; thus, when the FEA potential is lower, the focusing capability of the ECE is weaker, and the electron beam is mainly focused by the focusing electrodes (FEA and FEB). If the FEB potential gradually increases, then the potential at the center of FEA and FEB increases, thereby weakening the focusing capability of the focusing electrodes and then making the focal spot size become larger. When the FEA potential is higher, the focusing capability of the focusing

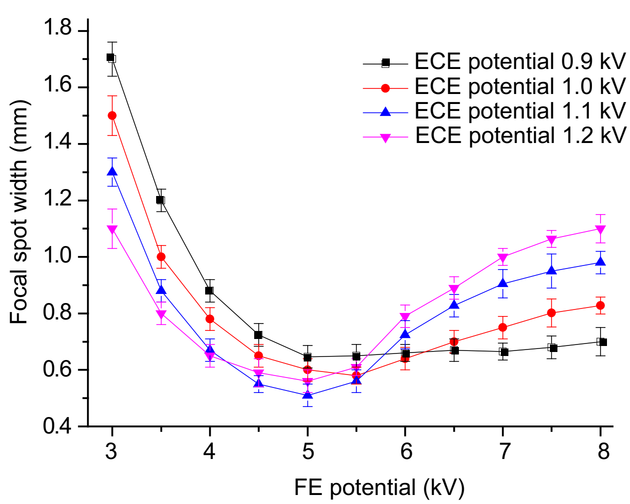

Fig. 12 (Color online) Focal spot width variation with FE potential at different ECE potentials (*X*-direction, FWHM)

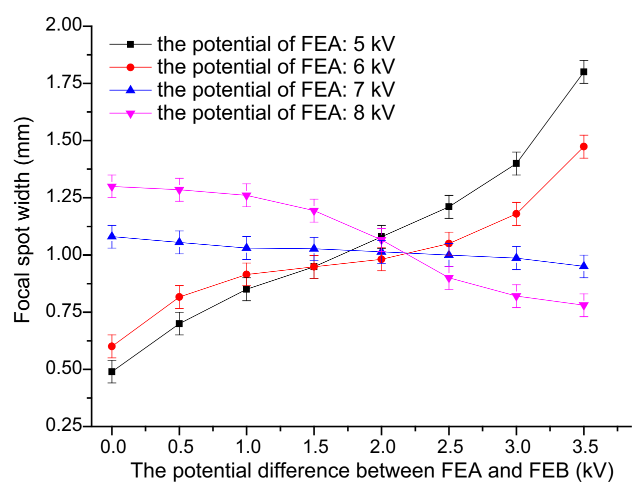

Fig. 13 (Color online) Focal spot width of deflection electron beam (*X*-direction, FWHM)

electrodes becomes weaker and that of the ECE shows an advantage. If the FEB potential increases gradually, then the ECE becomes more powerful in terms of focusing capability; thus, the focal spot becomes smaller. However, the optimal focal spot size of the deflected electron beam is larger than that of the non-deflected electron beam, regardless of how the system parameters are adjusted. Therefore, the system obtains the deflection amplitude at the price of the focal spot size. Figure 13 only shows the focal spot size in the *X*-direction. The size in the *Y*-direction is compressed by the inclination angle of the anode and remains at approximately 0.60 mm and thus is not illustrated.

Figures 9, 12, and 13 show that when the electron beam is non-deflected, the optimum focusing potential is 5.0 kV and the optimum focal spot size is less than 0.55 mm. When the deflection amplitude of the beam is approximately 10.5 mm, the optimum focal spot is approximately 0.85 mm, with FEA and FEB potentials of 8.0 and 11.0 kV, respectively. To obtain the optimal focal spot size with deflected and non-deflected electron beams, three high-voltage powers (5.0, 8.0, and 11.0 kV) are required, followed by rapidly switching through the insulated-gate bipolar transistor or reed relay. This process complicates the high-voltage power system and makes it costly. If the system is not extremely strict on the focal spot size, then two high-voltage powers can be used (7.0 and 10.0 kV). When the electron beam is not deflected, the FEA and FEB potentials are 7.0 kV and the focal spot is approximately 0.90 mm. When the electron beam is deflected, the FEA and FEB potentials are 7.0 and 10.0 kV, respectively. The deflection amplitude is approximately 10.5 mm, and the focal spot is approximately 1.00 mm. The focal spot is slightly larger, but it can satisfy most of the imaging requirements. At the same time, less focusing power allows for easier control of the system and cost efficiency.

4 Digital radiography performance

4.1 Dose distribution of multiple X-ray sources

Figure 14 shows the geometric structure used for the experimental study of the dose distributions of the multiple X-ray sources. Seven electron guns, with a spacing of 25 mm, are used on the experimental platform. The Ti-window width is 170 mm, and its center coincides with the focal spot of the fourth electron gun. The distance between the focal spot and the Ti-window is approximately 230 mm. The distance between the Ti-window and the flat plate detector is approximately 79 mm. In the experiment, the electron gun emits electrons and generates an X-ray in turn, and the dose distribution of the X-ray is measured by the flat panel detector.

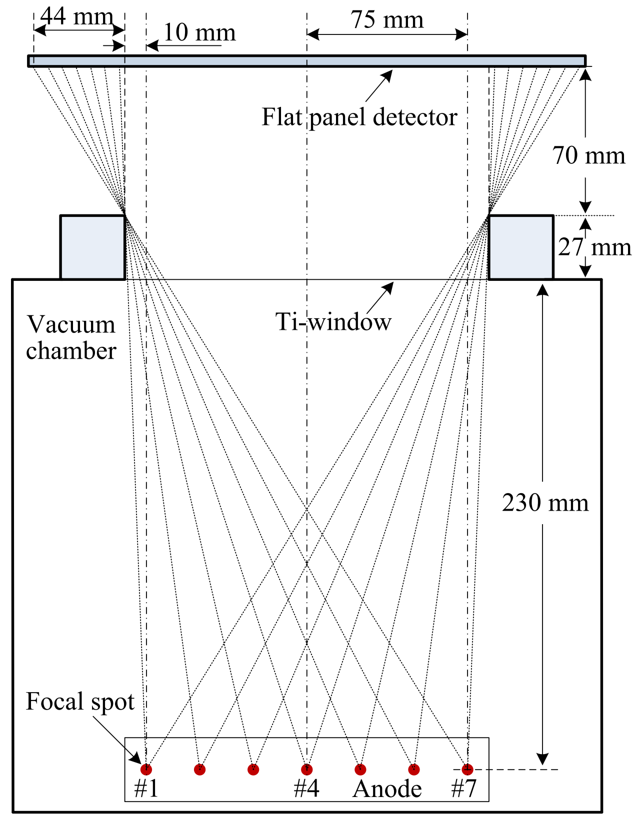

Fig. 14 Geometric structure of the multiple X-ray sources

Given that the X-ray is absorbed by the mechanical structure, only an X-ray passing through the Ti-window can be detected by the detector, resulting in a small radiation angle of approximately 35.5° (Fig. 14). The dose distribution is roughly symmetrical at the center (the position of electron gun #4). That is, the dose distributions of electron guns #1 and #7, #2 and #6, and #3 and #5 are roughly symmetric. Within the range of the dose coverage, the dose of a single gun varies greatly. However, due to the symmetrical dose distribution, the cumulative dose distribution of multiple guns varies very little, as shown in the average line in Fig. 15. The experimental conditions are an anode voltage of 160 kV, a beam current of 15 mA, and a dose of 1.5 mA ms.

4.2 Modulation transfer function (MTF)

The MTF is measured according to the edge method recommended by the IEC-62220 standard. The detector is a PaxScan 2520DX flat panel detector from Varian. The radiation quality is approximately RQA9, the actual exposure voltage is 160 kV, and the dose is approximately 0.1 mA S. The focal spot-detector distance is

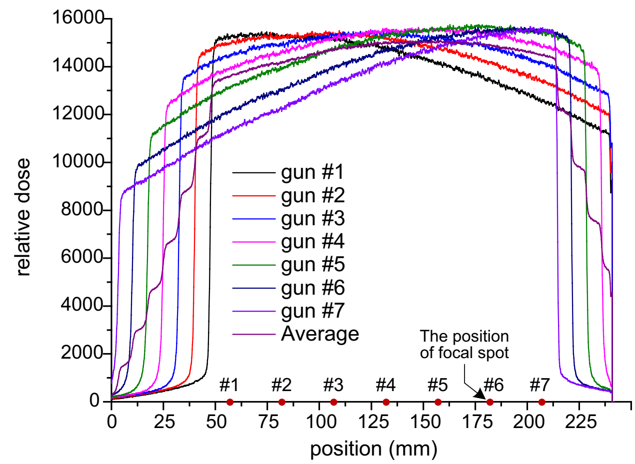

Fig. 15 (Color online) Dose distribution of the multiple X-ray sources

approximately 1000 mm, and the focal spots in the x- and y-directions are 0.4 mm and 0.55 mm, respectively. The blade edge is made of tungsten with a thickness of 1.6 mm and is placed on the detector surface at an angle of approximately 3° to the detector edge. The image data are measured by the detector using oversampling projection to obtain the edge spread function (ESF). Then, the ESF is derived to obtain the line spread function. Finally, a Fourier transform is performed to obtain the MTF [22]. Figure 16 shows the experimental results in the x- and y-directions. The difference of the MTFs in the two orthogonal axes is attributed to the anisotropy of the focal spot size. When the resolution at which the MTF is 0.05 is the limit resolution of the system, the limit resolutions in the x- and y-directions are approximately 2.85 cycles/mm and 3.00 cycles/mm, respectively.

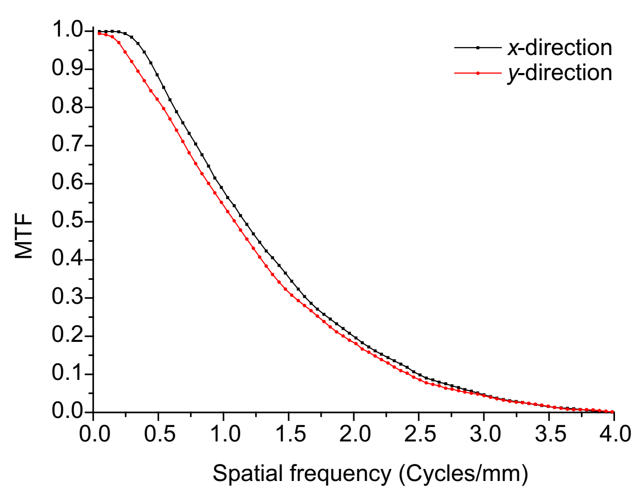

Fig. 16 (Color online) Modulation transfer function estimate of the system

4.3 Noise power spectrum (NPS)

The NPS is measured using the same geometric conditions and exposure parameters as those measured of the MTF. The obtained image is divided into regions of interest (ROIs) of size 256 × 256. Two adjacent ROIs overlap by 128 pixels, and the total coverage area is approximately 130 mm × 130 mm. Given the heel effect of the source, the inverse relation between the dose and the square of the distance, and the difference of the detector pixels, a low-frequency background trend is formed on the quantum random noise [23]. Therefore, during data processing, the low-frequency background trend is removed by subtracting a 2-D second-order fit of the image at first [23, 24]. Then, the Fourier transform is performed and standardized to obtain the NPS. Figure 17 shows the experimental results of the NPS. The NPS has the same trends in the x- and y-directions, and the low-frequency noise is slightly larger than the high-frequency noise.

5 Imaging experiment

Figure 18 shows an X-ray radiograph of a line-pair (LP) gauge standard. The experimental conditions are an anode voltage of 160 kV and a beam current of 30 mA. The detector system adopts a flat panel detector with a resolution of 127 μm, the focal spot size is approximately 0.40 mm, and the geometric magnification is approximately 1.8 times. The highest spatial frequency that can be resolved by the eye is approximately 3.4 LP/mm [25].

Figure 19 shows the X-ray images of a FPGA (EP4CE6E22C8N) chip. Figure 19a shows the photograph of the FPGA. The chip size is 22 mm × 22 mm, the total number of pins is 144, the center pitch of the pins is 0.5 mm, and the width of the pins is 0.25 mm. Figure 19b shows the X-ray image of the chip. The X-ray passes through the plastic mold and has an excellent imaging effect on the internal structure of the chip. The pins of the chip, the gold wire (smallest at approximately 0.1 mm), the lead frame, and the integrated circuit die inside the chip are very clear. These results are indicative of a small focal spot. The experimental conditions are an anode voltage of 160 kV, a beam current of 30 mA, a focal spot size of approximately 0.40 mm × 0.55 mm, and a resolution of the detector system of 25 μm.

The electron gun operates in pulsed mode to capture an X-ray image of the moving objects. A 100-mm-diameter rotating metal disk is chosen to demonstrate the fast pulse capability of the sources. Figure 20 shows the photographs and X-ray radiographs of the metal disk in stationary and moving states. The rotation rate in revolutions per minute, beam current, and pulse width are shown in detail in

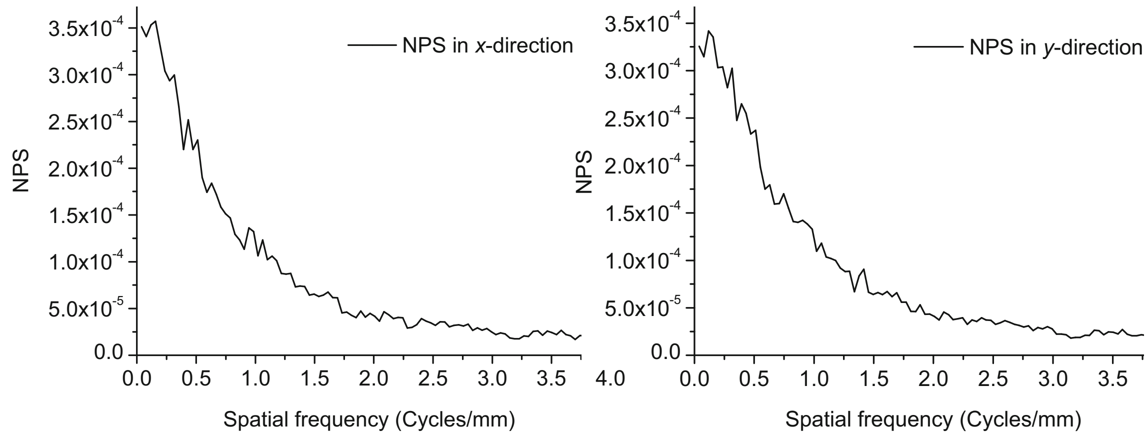

Fig. 17 Noise power spectrum estimate of the system

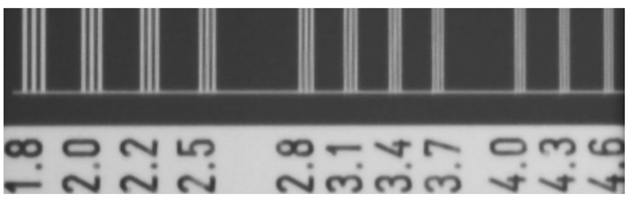

Fig. 18 Line-pair gauge X-ray radiograph

Fig. 20. The speeds of the blade tip of the metal disk in Fig. 20d–f are 10, 44, and 44 m/s, respectively. The X-ray image becomes blurred as the metal disk speed increases. Figure 20e, f shows that when the metal disk is rotating at high speed, reducing the pulse width helps clear the imaging. This phenomenon is due to the fact that when the pulse width is 20 μs, the motion distance of the blade tip is

Fig. 19 FPGA chip X-ray image (**a** the chip photograph, **b** the X-ray image, **c**, **d** the detail of the image)

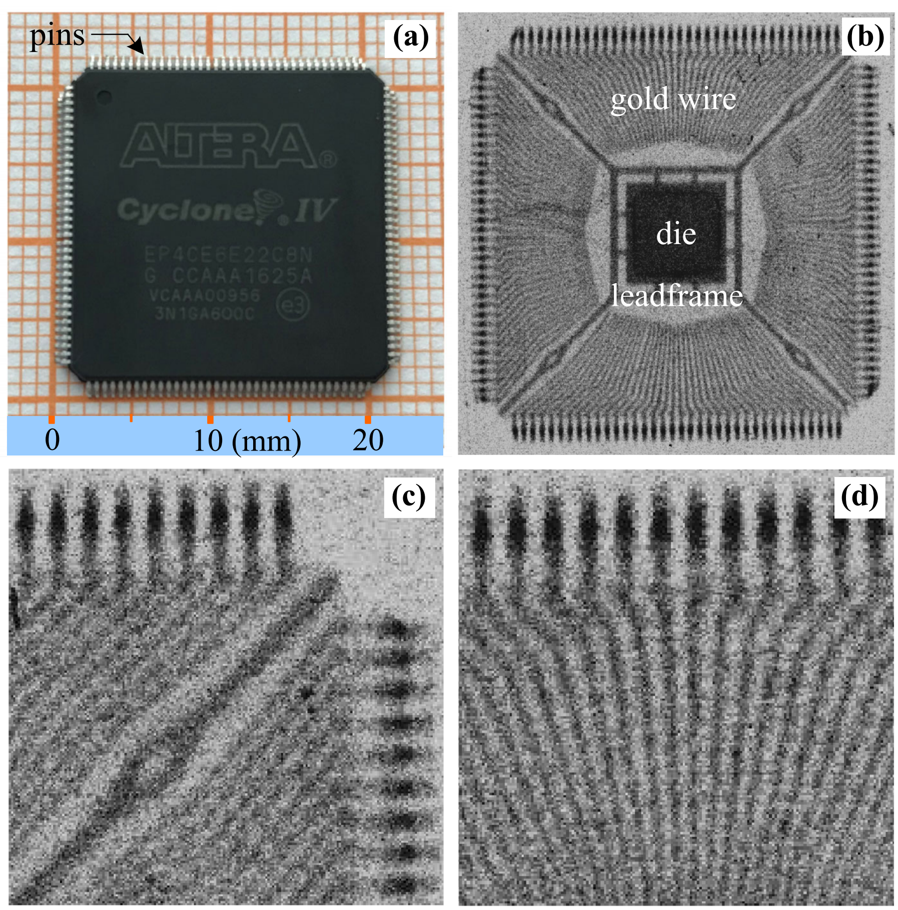

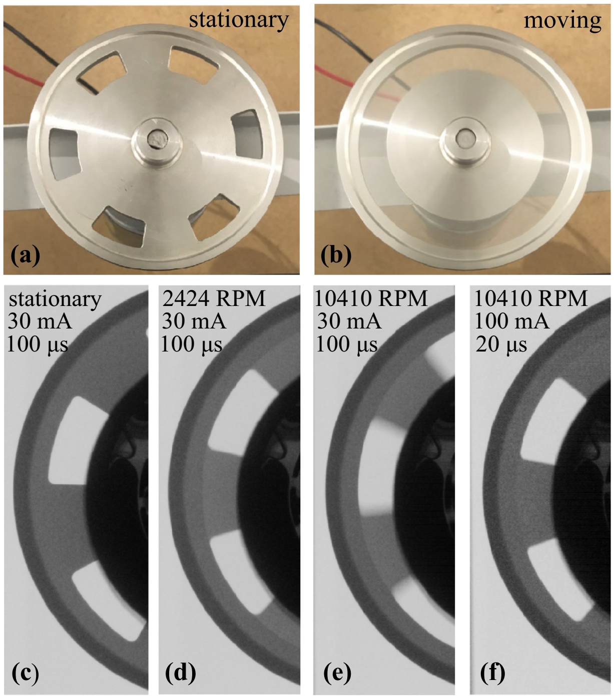

Fig. 20 (Color online) Photographs (top) and X-ray images (bottom) of the metal disk using a single X-ray pulse

less than 0.8 mm. Hence, the multisource combination of a higher beam current and fast pulse control allows it to "freeze" rapidly moving objects and get a clear X-ray radiograph. The experimental conditions are an anode voltage of 160 kV and a focal spot size of approximately 0.40 mm × 0.55 mm. The detector system adopts a flat panel detector with a resolution of 127 µm.

6 Conclusion and discussion

Compared with traditional spiral CT, stationary CT features a simple structure, fast scanning, a high contrast ratio, a clear image, and good stability. Distributed X-ray sources provide a solid foundation for the invention of stationary CT. In this study, a beam deflection electron gun for distributed sources is designed. The gun uses a dispenser cathode as the electron emission unit, a grid mesh to control the beam current, and two electrostatic lenses for beam shaping, focusing, and deflection. Simulation and experimental results suggest that the electron gun satisfies the requirements of most imaging applications and provides more possibilities and options for distributed X-ray sources and stationary CT. The experimental results show that both the deflected election beam and non-deflected election beam obtain a better focal spot, which has an excellent imaging effect on the FPGA chip. The experiments on the rotating metal disk show that the source has a good time resolution and an excellent imaging effect on the rotating metal disk. In our future research, we will use 33 electron guns to design 99 X-ray distributed sources.

References

1. R.A. Robb, E.A. Hoffman, L.J. Sinak et al., High-speed three-dimensional X-ray computed tomography: the dynamic spatial reconstructor. Proc. IEEE **71**, 3 (1983). https://doi.org/10.1109/PROC.1983.12589
2. Y.F. Yang, D.H. Zhang, K.D. Huang et al., Three-dimensional weighting reconstruction algorithm for circular cone-beam CT under large scan angles. Nucl. Sci. Tech. **27**, 116 (2017). https://doi.org/10.1007/s41365-017-0262-3
3. G. Wang, T.H. Lin, P.C. Cheng et al., A general cone beam reconstruction algorithm. IEEE Trans. Med. Imaging **12**, 486–496 (1993). https://doi.org/10.1109/42.241876
4. C. Zhang, X.D. Pan, H.J. Shang et al., Improvements to conventional X-ray tube-based cone-beam computed tomography system. Nucl. Sci. Tech. **29**, 43 (2018). https://doi.org/10.1007/s41365-018-0370-8
5. W.A. Kalender, Thin-section three-dimensional spiral CT: is isotropic imaging possible. Radiology **197**, 578–580 (1995). https://doi.org/10.1148/radiology.197.3.7480719
6. P. Michael, B. D. Man, B. Kristiaan, Stationary computed tomography system and method. U.S. Patent 7 280 631, Oct. 9, 2007
7. V.B. Neculaes, P.M. Edic, M. Frontera et al., Multisource X-ray and CT: lessons learned and future outlook. IEEE Access **2**, 1568–1585 (2014). https://doi.org/10.1109/ACCESS.2014.2363949
8. G. Wang, H.Y. Yu, B.D. Man, An outlook on X-ray CT research and development. Med. Phys. **35**, 1051–1064 (2008). https://doi.org/10.1118/1.2836950
9. R. Behling, Medical X-ray sources now and for the future. Nucl. Instrum. Methods A. **873**, 43–50 (2017). https://doi.org/10.1016/j.nima.2017.05.038
10. C.A. Spindt, A thin-film field-emission cathode. J. Appl. Phys. **39**, 3504 (1968). https://doi.org/10.1063/1.1656810
11. C.A. Spindt, I. Brodie, L. Humphrey et al., Physical properties of thin-film field emission cathodes with molybdenum cones. J. Appl. Phys. **47**, 5248 (1976). https://doi.org/10.1063/1.322600
12. P.R. Schwoebel, J.M. Boone, J. Shao, Studies of a prototype linear stationary X-ray source for tomosynthesis imaging. Phys. Med. Biol. **59**, 2393–2413 (2014). https://doi.org/10.1088/0031-9155/59/10/2393
13. X.S. Wang, Q.Q. Li, J. Xie et al., Fabrication of ultralong and electrically uniform single-walled carbon nanotubes on clean substrates. Nano Lett. **9**, 3137–3141 (2009). https://doi.org/10.1021/nl901260b
14. X. Qian, A. Tucker, E. Gidcumb et al., High resolution stationary digital breast tomosynthesis using distributed carbon nanotube X-ray source array. Med. Phys. **39**, 2090–2099 (2012). https://doi.org/10.1118/1.3694667
15. G. Yang, R. Rajaram, G.H. Cao et al., Stationary digital breast tomosynthesis system with a multi-beam field emission X-ray source array, in *Proceedings of SPIE. 6913, Medical Imaging 2008: Physics of Medical Imaging, 69131A* (2008). http://dx.doi.org/10.1117/12.770622
16. F. Sprenger, X. Calderon, Y. Cheng et al., Distributed source X-ray tube technology for tomosynthesis imaging, in *Proceedings*

of SPIE, 7622, Medical Imaging 2010: Physics of Medical Imaging, 76225M (2010). https://doi.org/10.1117/12.844586
17. J.M. Bonard, C. Klinke, K.A. Dean et al., Degradation and failure of carbon nanotube field emitters. Phys. Rev. B. **67**, 115406 (2003). https://doi.org/10.1103/PhysRevB.67.115406
18. X.C. Xu, J. Kim, P. Laganis et al., A tetrahedron beam computed tomography benchtop system with a multiple pixel field emission X-ray tube. Med. Phys. **38**, 5500–5508 (2011). https://doi.org/10.1118/1.3634043
19. V.B. Neculaes, Y. Zou, P. Zavodszky et al., Design and characterization of electron beam focusing for X-ray generation in novel medical imaging architecture. Phys. Plasmas **21**, 056702 (2014). https://doi.org/10.1063/1.4872033
20. K. Frutschy, B.D. Man, P. Edic et al., X-ray Multisource for Medical Imaging, in *Proceeding of SPIE. 7258, Medical Imaging 2009, Physics of Medical Imaging; 725822* (2009). https://doi.org/10.1117/12.812043
21. V.B. Neculaes, A. Caiafa, Y. Cao et al., Multisource inverse-geometry CT. Part II. X-ray source design and prototype. Med. Phys. **43**, 4617–4627 (2016). https://doi.org/10.1118/1.4954847
22. L. Lanca, A. Silva, *Digital Imaging Systems for Plain Radiography* (Springer, New York, 2013), pp. 25–30. https://doi.org/10.1007/978-1-4614-5067-2
23. Z. Zhou, F. Gao, H. Zhao et al., Effect of background trends removal on noise power spectrum measurements in digital X-ray imaging, in *Proceeding of SPIE. 7890, Advanced Biomedical and Clinical Diagnostic Systems IX; 78901F* (2011). http://dx.doi.org/10.1117/12.871053
24. J.T. Dobbins III, E. Samei, N.T. Ranger et al., Intercomparison of methods for image quality characterization. II. Noise power spectrum. Med. Phys. **33**, 1466–1475 (2006). https://doi.org/10.1118/1.2188819
25. J.T. Bushberg, J.A. Seibert, E.M. Leidholdt et al., *The Essential Physics of Medical Imaging*, 2nd edn. (Lippincott Williams and Wilkins, Philadelphia, 2002), pp. 31–44. https://doi.org/10.1007/s00259-002-1073-1